Journal of the Optical Society of America B
OPTICAL PHYSICS

Mode coupling at avoided crossings in slab waveguides with comparison to optical fibers: tutorial

J. T. Young,[1] C. Wei,[2] C. R. Menyuk,[3] and J. Hu[1,*]

[1]Baylor University, One Bear Place, Waco, Texas 76798, USA
[2]University of Mary Hardin-Baylor, 900 College Street, Belton, Texas 76513, USA
[3]University of Maryland Baltimore County, 1000 Hilltop Circle, Baltimore, Maryland 21270, USA
*Corresponding author: jonathan_hu@baylor.edu

Received 2 August 2021; revised 23 September 2021; accepted 24 September 2021; posted 28 September 2021 (Doc. ID 435828); published 26 October 2021

Avoided crossings are important in many waveguides and resonators. That is particularly the case in modern-day solid-core and air-core optical fibers that often have a complex geometry. The study of mode coupling at avoided crossings often leads to a complicated analysis. In this tutorial, we aim to explain the basic features of avoided crossings in a simple slab waveguide structure so that the modes can be found analytically with simple sinusoidal and exponential forms. We first review coupled-mode theory for the guided mode in a slab waveguide, which has a higher index in the core. We study the effective index of the guided true mode for a five-layer slab waveguide including two core layers with higher indices compared to the indices in the three cladding layers. Then, we study the same structure by using the overlap between approximate modes confined in the two individual core slabs. When the two individual core slabs are not near each other, the avoided crossing using the true modes within the two-slab waveguide agrees well with the results using the overlap between the two approximate modes. We also study coupled-mode theory and avoided crossings for leaky modes in an antiresonant slab waveguide. We obtain good agreement between the results using the true leaky mode and the results using the overlap between approximate modes. We then discuss examples of avoided crossings in solid-core and air-core optical fibers. We describe the similarities and differences between the optical fibers and simple slab waveguides that we have analyzed in detail.

https://doi.org/10.1364/JOSAB.435828

1. INTRODUCTION

Avoided crossings between modes appear in many optical waveguides and resonators. They often occur between modes in a single waveguide or resonator, or due to coupling between modes in different waveguides or resonators that are in close proximity. The study of mode coupling in hollow-core fibers often leads to a complicated analysis, because the modes experiencing avoided crossings in hollow-core fibers are leaky modes [1], which require a computational solution due to the complex structures. Leaky modes and avoided crossings have long been studied in optical systems. While the theory of avoided crossing is well understood in the case of guided modes in optical waveguides, there has been little or no study of avoided crossings in optical waveguides that have leaky modes and whose structures are sufficiently simple for the modes to be derived analytically. In this tutorial, we focus on one-dimensional slab waveguides to study the avoided crossings for leaky modes in a simple context. The formulation of coupled-mode analysis has been presented in [2]. This formulation of coupled-mode theory applies to guided modes, and it cannot be directly applied to leaky modes. We describe here the revision of coupled-mode equations that is necessary to describe leaky modes in one-dimensional slab waveguides.

Optical waveguides can be divided into two categories: one-dimensional waveguides and two-dimensional waveguides. The slab or planar waveguides in one-dimensional structures appear in a wide range of applications, including photonic-integrated circuits (PICs). PICs may make possible high-throughput and low-power signal processors that overcome the limits of conventional electronic digital signal processing technology [3]. One-dimensional PIC structures have been studied, but no detailed study of avoided crossings has been carried out using slab waveguides. Avoided crossings can play an important role in the mode coupling in silicon PICs [4]. Recently, hollow-core optical fibers that are two-dimensional waveguides have been widely studied and can have low loss values around 0.5 dB/km [5–11]. These fibers can be designed so that most of the power is transmitted through an air core with low loss and low

nonlinearity. As a result, hollow-core fibers are useful for a variety of applications, such as high-power delivery [12], biological applications [13,14], gas lasers [15–17], and supercontinuum generations [18]. In air-core optical fibers, such as negative curvature fibers, the fundamental core mode couples strongly to additional core and cladding modes in certain conditions. The analysis of avoided crossings using antiresonant glass partitions can provide insight into the mode coupling and loss of the core mode in negative curvature fibers [19–21]. If the glass partition thickness corresponds to antiresonance in the slab waveguide, then the fundamental mode loss is low. In this case, the width of the avoided crossing, which is defined as the minimum difference in effective indices of the coupled modes, is small due to weak coupling. When the glass thickness corresponds to resonance, there is a larger avoided crossing width, and the fundamental mode experiences a higher loss. In addition, mode coupling and avoided crossings are important in understanding the efficiency of ring resonators, which have been successfully used for filters, biosensing, and frequency comb generations [22].

Avoided crossings, also known as anticrossings, were first described in quantum mechanics by Neumann and Wigner, who showed that energy levels of electronic states cannot cross [23]. Avoided crossings have also been used to explain the nonintersection of electron energy states for different molecules [24,25]. The first discussion of avoided crossings in optics was made in 1963 by Eck *et al.* in their study of fluorescence [26]. In 1979, Marcuse and Kaminow observed avoided crossings of transverse electric (TE) and transverse magnetic (TM) modes within a thin-film slab waveguide [27]. The first study of avoided crossings in optical fibers was carried out in 1988 in a fiber-optic ring resonator [28]. More recently, avoided crossings have become important in understanding the coupling between the core and cladding modes in solid-core photonic crystal fibers [29], photonic bandgap fibers (PBGFs) [30–34], negative curvature fibers [19–21], and kagome fibers [35]. In high-power laser systems using a photonic crystal fiber, it was later found that the avoided crossing induced by the pump profile, bending, or index depression may lead to unwanted deformations of the output beam [29]. On the other hand, avoided crossings have been used for optical filters [36], refractive index sensors [37–39], temperature sensors [40], and higher-order mode (HOM) suppression [19,41,42].

The rest of this tutorial is organized as follows: in Section 2, we review the equations for the coupled-mode theory for the guided mode in a high-index core slab waveguide. Section 3 describes an example of a guided mode in a slab waveguide, where the index of core, n_g, is larger than the index of cladding, n_c. We compare the computationally exact results, computed using the finite difference method (FDM), to the results from coupled-mode theory. Section 4 describes the derivation of the coupled-mode theory for leaky modes in an antiresonant slab waveguide. Section 5 shows an example of mode coupling in an antiresonant slab waveguide. We again compare the computationally exact results to the results from coupled-mode theory. In Section 6, we discuss how the insights that we have gained can be applied to more complex geometries, and we conclude in Section 7.

2. COUPLED-MODE THEORY FOR GUIDED MODES IN A SLAB WAVEGUIDE WITH $n_g > n_c$

We start with a description of the guided modes in a one-dimensional five-layer slab waveguide with two core layers and three cladding layers, shown in Fig. 1(a). The refractive index of the two guiding layers is n_g, and the refractive index of the surrounding layers is n_c. To have guided modes, we must have $n_g > n_c$. The thicknesses of the guiding layers are t_1 and t_2. In coupled-mode theory, we decouple the two guiding layers by considering the modes in two waveguides, each of which has one guiding layer, corresponding to one of the two guiding layers in the original waveguide, labeled waveguide 3 in Fig. 1(b).

The refractive index distributions for waveguides 1, 2, and 3 are denoted by $n_1(x)$, $n_2(x)$, and $n_3(x)$, respectively, and may be written as

$$\begin{aligned} n_1^2(x) &= n_c^2 + n_-^2(x), \\ n_2^2(x) &= n_c^2 + n_+^2(x), \\ n_3^2(x) &= n_c^2 + n_-^2(x) + n_+^2(x), \end{aligned} \tag{1}$$

where $n_+^2(x)$ and $n_-^2(x)$ are defined as

$$\begin{aligned} n_+^2(x) &= \begin{cases} n_g^2 - n_c^2 & g/2 < x < g/2 + t_2 \\ 0 & \text{otherwise} \end{cases}, \\ n_-^2(x) &= \begin{cases} n_g^2 - n_c^2 & -t_1 - g/2 < x < -g/2 \\ 0 & \text{otherwise} \end{cases}. \end{aligned} \tag{2}$$

We will focus on TE modes. In this case, the field component E_y obeys the Helmholtz equation

$$\frac{\partial^2 E_y}{\partial z^2} + \frac{\partial^2 E_y}{\partial x^2} + \frac{n^2(x)\omega_0^2}{c^2} E_y = 0. \tag{3}$$

If we consider one mode in waveguide 1 with a normalized transverse profile $\psi_1(x)$ and wavenumber β_1 and one mode in waveguide 2 with normalized transverse profile $\psi_2(x)$ and wavenumber β_2, then there is a propagating electric field in waveguide 3 that may be written approximately as

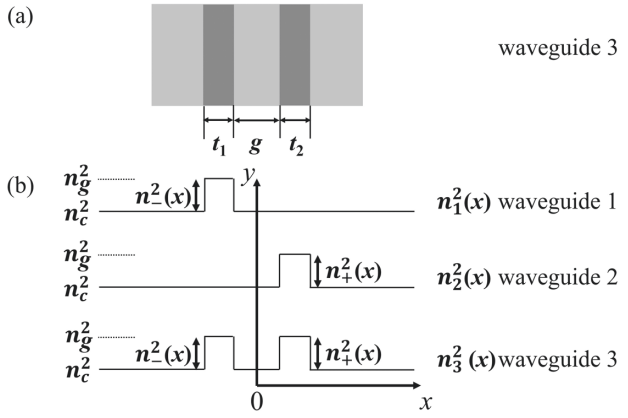

Fig. 1. (a) Illustration of the two-core index-guided waveguide structure. (b) Illustration of the refractive index profiles for waveguides 1, 2, and 3.

$$E_y(x,z,t) = A_1(z)\psi_1(x)\exp[i(\omega_0 t - \beta_1 z)] + A_2(z)\psi_2(x)\exp[i(\omega_0 t - \beta_2 z)]. \quad (4)$$

Transverse mode profiles $\psi_1(x)$ and $\psi_2(x)$ are normalized so that $\int_{-\infty}^{\infty}|\psi_{1,2}|^2 dx = 1$. Parameters $A_1(z)$ and $A_2(z)$ are slowly varying amplitudes for waveguides 1 and 2 respectively, so that

$$-\beta_1^2\psi_1 + \frac{\partial^2\psi_1}{\partial x^2} + \frac{n_1^2(x)\omega_0^2}{c^2}\psi_1 = 0,$$
$$-\beta_2^2\psi_2 + \frac{\partial^2\psi_2}{\partial x^2} + \frac{n_2^2(x)\omega_0^2}{c^2}\psi_2 = 0. \quad (5)$$

Substituting Eq. (4) into Eq. (3) and using Eq. (5) with the slowly varying envelope approximation so that $|\partial^2 A_{1,2}/\partial z^2| \ll \beta_{1,2}|\partial A_{1,2}/\partial z|$, we obtain

$$-2i\beta_1\psi_1\frac{\partial A_1}{\partial z}\exp(-i\beta_1 z) - 2i\beta_2\psi_2\frac{\partial A_2}{\partial z}\exp(-i\beta_2 z) + \frac{n_+^2(x)\omega_0^2}{c^2}A_1\psi_1\exp(-i\beta_1 z) + \frac{n_-^2(x)\omega_0^2}{c^2}A_2\psi_2 \times \exp(-i\beta_2 z) = 0. \quad (6)$$

We now multiply the above equation by $\psi_1^*(x)$ and $\psi_2^*(x)$, integrate over x, and use the normalized fields, yielding two equations:

$$\frac{\partial A_1}{\partial z} + \frac{i\kappa_{12}}{2\beta_1}A_2\exp[i(\beta_1-\beta_2)z] = 0,$$
$$\frac{\partial A_2}{\partial z} + \frac{i\kappa_{21}}{2\beta_2}A_1\exp[-i(\beta_1-\beta_2)z] = 0, \quad (7)$$

where

$$\kappa_{11} = \frac{\omega_0^2}{c^2}\int_{-\infty}^{\infty} n_+^2(x)|\psi_1(x)|^2 dx,$$
$$\kappa_{12} = \frac{\omega_0^2}{c^2}\int_{-\infty}^{\infty} n_-^2(x)\psi_1^*(x)\psi_2(x) dx,$$
$$\kappa_{21} = \frac{\omega_0^2}{c^2}\int_{-\infty}^{\infty} n_+^2(x)\psi_1(x)\psi_2^*(x) dx,$$
$$\kappa_{22} = \frac{\omega_0^2}{c^2}\int_{-\infty}^{\infty} n_-^2(x)|\psi_2(x)|^2 dx. \quad (8)$$

In the derivation, we assume that $\psi_1(x)$ and $\psi_2(x)$ are well confined in the individual waveguides, so that $\int_{-\infty}^{\infty}\psi_1^*(x)\psi_2(x)dx \ll 1$, $\kappa_{11} \ll \kappa_{12}$, and $\kappa_{22} \ll \kappa_{21}$. The amplitudes in the individual waveguides can be written as

$$A_1 = R_1\exp[i\Delta\beta z/2], A_2 = R_2\exp[-i\Delta\beta z/2], \quad (9)$$

where $\Delta\beta = \beta_1 - \beta_2$, while R_1 and R_2 are slowly varying quantities. Using Eq. (9), we can rewrite Eq. (7) in matrix form as

$$\frac{d\mathbf{R}}{dz} = i\lambda\mathbf{R} = -i\begin{bmatrix}\Delta\beta/2 & \kappa_{12}/(2\beta_1)\\ \kappa_{21}/(2\beta_2) & -\Delta\beta/2\end{bmatrix}\mathbf{R}, \quad (10)$$

where $\mathbf{R}$ can be written as

$$\mathbf{R} = \begin{bmatrix}V_1\\ V_2\end{bmatrix}e^{i\lambda z} = \mathbf{V}e^{i\lambda z}. \quad (11)$$

Equation (10) is a standard matrix algebra eigenvalue problem, where $\mathbf{V}$ is the eigenvector. The condition for a nontrivial solution for $\mathbf{V}$ is that the determinant of the matrix must vanish. We then find

$$-\frac{(\Delta\beta)^2}{4} + \lambda^2 - \frac{\kappa_{12}\kappa_{21}}{4\beta_1\beta_2} = 0, \quad (12)$$

which yields the solution $\lambda_{1,2}$, where

$$\lambda_{1,2} = \mp\frac{1}{2}\left[(\Delta\beta)^2 + \frac{\kappa_{12}\kappa_{21}}{\beta_1\beta_2}\right]^{1/2}. \quad (13)$$

According to Eq. (11), the corresponding normalized eigenvectors are

$$\begin{bmatrix}V_1\\ V_2\end{bmatrix} = \begin{bmatrix}-\kappa_{12}\\ \beta_1(\Delta\beta + 2\lambda)\end{bmatrix}/\{\kappa_{12}^2 + [\beta_1(\Delta\beta + 2\lambda)]^2\}^{1/2}. \quad (14)$$

When $\Delta\beta \gg \kappa_{12}, \kappa_{21}$, we find that $\lambda_{1,2} = \mp\Delta\beta/2$, and the solutions for $\mathbf{V}$ are (0,1) or (1,0), which means the two solutions are entirely in waveguide 2 or waveguide 1. When $\Delta\beta = 0$, we find that $\beta_1 = \beta_2$ and $\kappa_{12} = \kappa_{21}$, yielding the solutions of (1/2, 1/2) or (−1/2, 1/2) for $\mathbf{V}$; hence, the solution in field intensity is nearly equal in both waveguides.

Using Eqs. (4), (9), and (11), the field in waveguide 3 may be written as

$$E_y(x,z,t) = V_1\psi_1(x)\exp[i(\omega_0 t - \beta_1' z)] + V_2\psi_2(x)\exp[i(\omega_0 t - \beta_2' z)], \quad (15)$$

with

$$n_{\text{eff1}} = \beta_1'/k_0 = \frac{1}{k_0}\left(\frac{\beta_1+\beta_2}{2} - \lambda_1\right),$$
$$n_{\text{eff2}} = \beta_2'/k_0 = \frac{1}{k_0}\left(\frac{\beta_1+\beta_2}{2} - \lambda_2\right), \quad (16)$$

where k_0 is the wavenumber, and $n_{\text{eff1,2}} = \beta_{1,2}'/k_0$ are the effective indices of the two modes that we are considering. We now obtain the width of the avoided crossing when $\beta_1 = \beta_2$ and $\Delta\beta = 0$:

$$\delta = |n_{\text{eff1}} - n_{\text{eff2}}| = \frac{1}{k_0}\left(\frac{\kappa_{12}\kappa_{21}}{\beta_1\beta_2}\right)^{1/2}, \quad (17)$$

which we define as the minimum difference in effective indices for the two modes in waveguide 3. Coupling coefficients κ_{12} and κ_{21} are given in terms of the approximate modes according to Eq. (8). We have thus found that the refractive indices of the true modes and the avoided crossing in waveguide 3 can be approximately obtained using the refractive indices and mode profiles of the modes of waveguides 1 and 2.

3. EXAMPLE OF MODE COUPLING IN A SLAB WAVEGUIDE WITH GUIDED MODES

In this section, we will use the equations from Section 2 to study the mode coupling between the fundamental modes in the

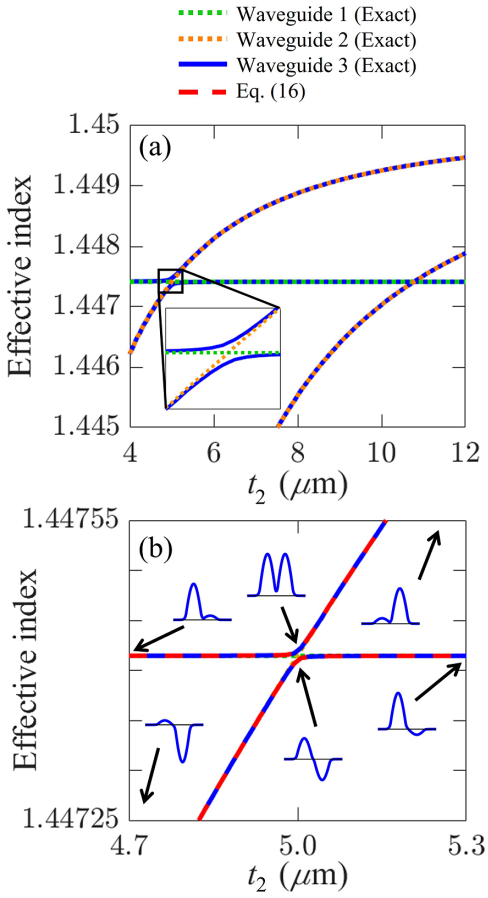

Fig. 2. (a) Effective index for the fundamental core mode in waveguides 1 and 2 (dashed curves) and waveguide 3 (solid curve) as a function of t_2. Inset in (a) shows a magnified plot so that the avoided crossing may be easily seen. (b) Magnified plot in (a) around the first avoided crossing at $t_2 = 5$ μm. Insets show mode profiles in waveguide 3. The red dashed curve shows the effective index obtained from Eq. (16).

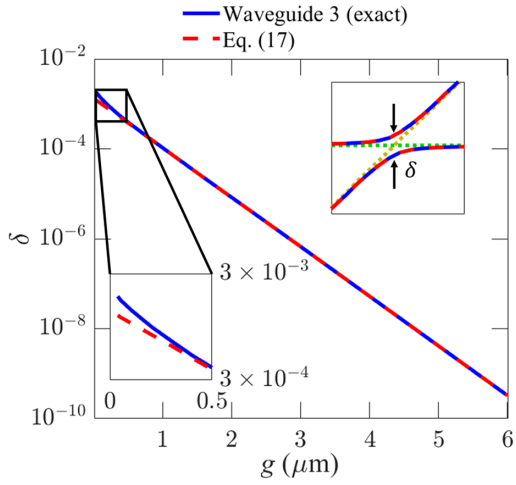

Fig. 3. Avoided crossing width calculated using the minimum difference in the effective index, δ, versus the gap separation in waveguide 3. The solid blue curve shows the computationally exact result, and the dashed red curve shows the approximate result from coupled-mode theory [Eq. (17)]. The top right inset shows a magnified plot of Fig. 2(b) to illustrate the avoided crossing at when $g = 2$ μm and $t_1 = t_2 = 5$ μm. The bottom left inset shows a magnified plot when g is between 0.04 and 0.5 μm.

five-layer slab waveguide with two core layers and three cladding layers (waveguide 3). We consider an example with $n_g = 1.45$ and $n_c = 0.96 n_g = 1.39$, which was previously studied [1]. The thickness of the first glass layer, t_1, is fixed at 5 μm. The wavelength is 1 μm. The gap between glass slabs, g, is fixed at 2 μm. We increase the thickness of the second glass layer, t_2, from 4 to 12 μm so that the avoided crossing can be observed. In Fig. 2(a), the solid blue curves show the effective indices of the modes in the two-layer slab waveguide 3, shown in Fig. 1. The dotted green curve shows the effective index for the fundamental mode of waveguide 1, which has a constant value of 1.44742. The dotted orange curves show the effective indices for the fundamental mode and the first high-order mode of waveguide 2, which has a changing thickness, t_2. We use the FDM to calculate the computationally exact modes and the effective indices.

In Fig. 2(a), the dotted curves for the effective index of the two single-layer waveguides overlap with the solid blue curves for the effective index of the two-layer waveguide, except within an avoided crossing region. An avoided crossing occurs when t_2 is 5.0 μm or 10.6 μm, and the modes in the two high-index glass layers couple. To show the avoided crossing clearly, the inset in Fig. 2(a) shows a magnified plot near the first avoided crossing so that the differences in the effective indices may be easily distinguished. The insets in Fig. 2(b) show the mode profiles in waveguide 3 for different t_2 thicknesses equal to 4.7, 5.0, and 5.3 μm near the first avoided crossing. When $t_2 < 5$ μm, the modes are well confined in one of the glass layers. When $t_2 = 5$ μm, where the avoided crossing occurs, the two modes become a hybrid even or odd mode, which is located in both of the two high-index layers. When $t_2 > 5$ μm, the coupling decreases and the two modes are again primarily located in one of the two glass waveguides. If we follow the modes along either of the continuous branches of the effective index, we see that the mode switches from one waveguide to the other. This mode-swapping is a characteristic feature of avoided crossings.

We now use Eq. (17) from coupled-mode theory to study the avoided crossing, as shown in the dashed red curves in Fig. 2(b). We found that the dashed red curves using Eq. (17) agree exactly with a computationally exact FDM calculation of the modes in waveguide 3. Hence, the overlap of approximate modes confined in waveguides 1 and 2 via coupled-mode theory can account for the avoided crossing and makes it possible to approximate the true modes in waveguide 3.

We now set $t_1 = t_2 = 5$ μm and vary the gap, g, between the core layers. We plot the difference in the effective indices during the avoided crossing, δ, between the fundamental mode in core layer 1 and the fundamental mode in core layer 2, in Fig. 3. The top right inset in Fig. 3 gives an illustration of δ, showing the minimum difference between effective indices of the modes in waveguide 3. The bottom left inset shows a magnified plot of δ for small gap sizes so that differences between the computationally exact result and the result from coupled-mode theory may be distinguished. The parameter δ can be used to quantify the width of the avoided crossing and the strength of coupling between modes. A larger avoided crossing corresponds to a stronger coupling. The value of δ decreases exponentially as g increases. As the gap between adjacent core layers increases, the overlap between modes decreases, leading to the decrease in

the avoided crossing width. For very small gaps, the agreement between the computationally exact result and the approximate result from Eq. (17) breaks down.

4. COUPLED-MODE THEORY FOR LEAKY MODES IN AN ANTIRESONANT SLAB WAVEGUIDE

In an antiresonant slab waveguide, the antiresonance condition is needed to guide the mode in the central air slab [43]. To satisfy the antiresonance condition, the phase difference in the directly transmitted transverse wave vector and transverse wave vector with an additional two reflections must be an odd multiple of π. The glass thickness required for the antiresonance condition is given by [43–45]

$$t = (m - 0.5)\lambda/[2(n_g^2 - n_0^2)^{1/2}], \tag{18}$$

where m is a positive integer. To study coupled-mode theory in a leaky, antiresonant slab waveguide, we consider the slab waveguide that we show in Fig. 4(a), which has two large air slabs surrounded by glass–air–glass layers. We use two closely spaced higher-index glass layers (a double glass partition) as a barrier between the mode-confining air slabs, denoted as $W_{\text{core1,2}}$, to reduce the mode content between cores 1 and 2. In negative curvature fibers [44], center modes are naturally separated from the cladding air modes. The negative curvature in the glass layer strongly confines the fundamental mode so that it has low loss. To achieve a similar confinement in the single-slab structures that we are considering, we have found that it is necessary to use the double glass partitions that we show in Fig. 4.

Antiresonant waveguides are waveguides in which a lower index or air core is surrounded by higher-index or glass barriers, which are then surrounded in turn by more lower-index or air regions [1]. These can then be surrounded by more barriers, leading to more complex structures. Slab waveguides with this structure are antiresonant reflecting optical waveguides (ARROWs) [43,46], and if the outside cladding layers are lower-index or air, then there are no completely confined modes, and the modes of the structure will all be leaky [1]. However, the modes can be well confined in the core with low leakage if an antiresonant condition is obeyed [43,44].

Similar to the five-layer slab waveguide simulations in Section 2, three structures are used to understand the coupling of adjacent air-core layers. The refractive index distributions for waveguides 1, 2, and 3 in Fig. 4(b) are given by $n_1(x)$, $n_2(x)$, and $n_3(x)$:

$$\begin{aligned} n_1^2(x) &= n_-^2(x) + n_m^2(x) + n_0^2, \\ n_2^2(x) &= n_+^2(x) + n_m^2(x) + n_0^2, \\ n_3^2(x) &= n_-^2(x) + n_+^2(x) + n_m^2(x) + n_0^2, \end{aligned} \tag{19}$$

where

$$n_+^2(x) = \begin{cases} n_g^2 - n_0^2 & (t + g/2 + W_{\text{core2}}) < x < (2t + g/2 + W_{\text{core2}}) \\ n_g^2 - n_0^2 & (2t + 3g/2 + W_{\text{core2}}) < x < (3t + 3g/2 + W_{\text{core2}}) \\ 0 & \text{otherwise} \end{cases},$$

$$n_-^2(x) = \begin{cases} n_g^2 - n_0^2 & -(3t + 3g/2 + W_{\text{core1}}) < x < -(2t + 3g/2 + W_{\text{core1}}) \\ n_g^2 - n_0^2 & -(2t + g/2 + W_{\text{core1}}) < x < -(t + g/2 + W_{\text{core1}}) \\ 0 & \text{otherwise} \end{cases},$$

$$n_m^2(x) = \begin{cases} n_g^2 - n_0^2 & -(g/2 + t) < x < -g/2 \\ n_g^2 - n_0^2 & g/2 < x < g/2 + t \\ 0 & \text{otherwise} \end{cases}. \tag{20}$$

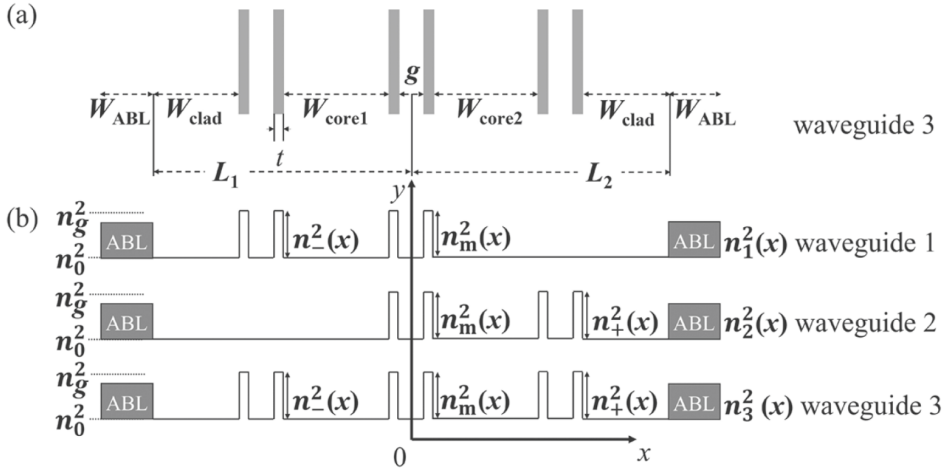

Fig. 4. (a) Illustration of the two-core antiresonant slab waveguide. (b) Definitions of refractive index profiles.

The field component E_y once again obeys the Helmholtz equation, Eq. (3); however, all the modes are leaky [1]. Absorbing boundary layers (ABLs) must be used to calculate the propagation constants in leaky waveguides, and the validity of this approach is described in detail in [1]. The field in the coupled structure with an index of $n_3(x)$ is approximated by Eq. (4). The TE field distributions and propagation constants for the modes in waveguides 1 and 2 are denoted by $\psi_1(x)$, $\psi_2(x)$, β_1, and β_2, respectively. The transverse field distributions $\psi_1(x)$ and $\psi_2(x)$ are the solutions to the wave equation in the corresponding waveguide with index distributions $n_1(x)$ and $n_2(x)$, which yields

$$\begin{aligned} -\beta_1^2\psi_1 + \frac{\partial^2\psi_1}{\partial x^2} + \frac{n_1^2(x)\omega_0^2}{c^2}\psi_1 = 0, \\ -\beta_2^2\psi_2 + \frac{\partial^2\psi_2}{\partial x^2} + \frac{n_2^2(x)\omega_0^2}{c^2}\psi_2 = 0. \end{aligned} \tag{21}$$

We normalize the transverse mode fields so that $\int_{-\infty}^{\infty}|\psi_{1,2}|^2 dx = 1$, which is possible once the absorbing layers are added and is feasible if the leakage power in the modes is small [1]. We carry out an analysis that is analogous to that in Section 2, and we find

$$\begin{aligned} \frac{\partial A_1}{\partial z} + \frac{i\kappa_{11}A_1}{2\beta_1} + \frac{i\kappa_{12}}{2\beta_1}A_2\exp[i(\beta_1-\beta_2)z] = 0, \\ \frac{\partial A_2}{\partial z} + \frac{i\kappa_{22}A_2}{2\beta_2} + \frac{i\kappa_{21}}{2\beta_2}A_1\exp[-i(\beta_1-\beta_2)z] = 0, \end{aligned} \tag{22}$$

where

$$\begin{aligned} \kappa_{11} &= \frac{\kappa_{11}^{+} - I_{12}\kappa_{21}^{+}}{1-|I_{12}|^2}, \\ \kappa_{12} &= \frac{\kappa_{12}^{-} - I_{12}\kappa_{22}^{-}}{1-|I_{12}|^2}, \\ \kappa_{21} &= \frac{\kappa_{21}^{+} - I_{12}^{*}\kappa_{11}^{+}}{1-|I_{12}|^2}, \\ \kappa_{22} &= \frac{\kappa_{22}^{-} - I_{12}^{*}\kappa_{12}^{-}}{1-|I_{12}|^2}, \\ \kappa_{11}^{+} &= \frac{\omega_0^2}{c^2}\int_{-\infty}^{\infty} n_{+}^2(x)|\psi_1(x)|^2 dx, \\ \kappa_{12}^{-} &= \frac{\omega_0^2}{c^2}\int_{-\infty}^{\infty} n_{-}^2(x)\psi_1^{*}(x)\psi_2(x) dx, \\ \kappa_{21}^{+} &= \frac{\omega_0^2}{c^2}\int_{-\infty}^{\infty} n_{+}^2(x)\psi_1(x)\psi_2^{*}(x) dx, \\ \kappa_{22}^{-} &= \frac{\omega_0^2}{c^2}\int_{-\infty}^{\infty} n_{-}^2(x)|\psi_2(x)|^2 dx, \\ I_{12} &= \int_{-\infty}^{\infty}\psi_1^{*}(x)\psi_2(x) dx. \end{aligned} \tag{23}$$

We note that I_{12} may not be negligible since there can be significant overlap within the two glass and air slabs that separate the air-core layers. We now introduce new variables $\tilde{A}_1$ and $\tilde{A}_2$ as

$$A_1 = \tilde{A}_1\exp\left(-\frac{i\kappa_{11}}{2\beta_1}z\right) \quad A_2 = \tilde{A}_2\exp\left(-\frac{i\kappa_{22}}{2\beta_2}z\right). \tag{24}$$

Equation (22) then becomes

$$\begin{aligned} \frac{\partial\tilde{A}_1}{\partial z} + \frac{i\kappa_{12}}{2\beta_1}\tilde{A}_2\exp[i(\Delta\beta)z] = 0, \\ \frac{\partial\tilde{A}_2}{\partial z} + \frac{i\kappa_{21}}{2\beta_2}\tilde{A}_1\exp[-i(\Delta\beta)z] = 0, \end{aligned} \tag{25}$$

where $\Delta\beta = \beta_1 - \beta_2 + \frac{\kappa_{11}}{2\beta_1} - \frac{\kappa_{22}}{2\beta_2}$. The amplitudes in the individual waveguides can be written as

$$\tilde{A}_1 = R_1\exp(i\Delta\beta z/2) \quad \tilde{A}_2 = R_2\exp(-i\Delta\beta z/2), \tag{26}$$

where R_1 and R_2 are slowly vary quantities. Substituting Eq. (26) into Eq. (25), we obtain the same matrix form as Eq. (10):

$$\frac{d\mathbf{R}}{dz} = i\lambda\mathbf{R} = -i\begin{bmatrix} \Delta\beta/2 & \kappa_{12}/(2\beta_1) \\ \kappa_{21}/(2\beta_2) & -\Delta\beta/2 \end{bmatrix}\mathbf{R}, \tag{27}$$

where $\mathbf{R}$ can be written as $e^{i\lambda z}[V_1\,V_2]^{\mathrm{T}}$, and T represents the matrix transpose operator. We may use the same procedure described by Eqs. (10)–(14) in Section 2 with a slightly changed β_1' and β_2'. The effective indices of the modes in waveguide 3 are given by

$$\begin{aligned} n_{\mathrm{eff1}} = \beta_1'/k_0 = \frac{1}{k_0}\left(\beta_1 + \frac{\kappa_{11}}{2\beta_1} - \frac{\Delta\beta}{2} - \lambda_1\right), \\ n_{\mathrm{eff2}} = \beta_2'/k_0 = \frac{1}{k_0}\left(\beta_2 + \frac{\kappa_{22}}{2\beta_2} + \frac{\Delta\beta}{2} - \lambda_2\right). \end{aligned} \tag{28}$$

Again, the width of the avoided crossing, defined as the minimum difference in effective indices for the modes in waveguide 3, is given by

$$\delta = |n_{\mathrm{eff1}} - n_{\mathrm{eff2}}| = \frac{1}{k_0}\left(\frac{\kappa_{12}\kappa_{21}}{\beta_1\beta_2}\right)^{1/2}, \tag{29}$$

which is the same as in Eq. (17), but with different expressions for κ_{12} and κ_{21} in Eq. (23). The refractive indices of the modes and the avoided crossing in the multi-layer slab waveguide can then be derived using the refractive indices and mode profiles of the approximate modes in the two single air-core antiresonant slab waveguides, just as we did with guided modes in Section 2.

5. MODE COUPLING IN ANTIRESONANT SLAB WAVEGUIDES

In this section, we will use the equations in Section 4 to study the mode coupling of the antiresonant slab waveguide in Fig. 4(a). According to the structures shown in Fig. 4, the thickness of the air-core layer in waveguide 1, W_{core1}, is fixed at 30 μm. The cladding thickness, W_{clad}, is fixed at 37 μm. The glass thickness, t, is fixed at 0.72 μm, which yields the antiresonance condition for a wavelength of 1 μm. The air gap, g, is set to 5 μm. An absorbing boundary condition was introduced in the simulation with a width of 150 μm. The index in the ABL is modeled as [1]

$$n(x) = n_0\left[1 + i\left(\frac{|x| - L_{1,2}}{W_{\mathrm{ABL}}}\right)^2 s\right]^{1/2}, \tag{30}$$

where n_0 is the index of air, W_{ABL} is the ABL thickness, and $L_{1,2}$ are the distances from the center to the beginning of the ABL as denoted in Fig. 4(a). We set $s = 6 \times 10^{-6}$ so that the mode field will decay as it reaches the edge of the simulation window. We increase W_{core2} from 20 to 70 μm so that the avoided crossings can be observed in waveguide 3. In Fig. 5(a), the effective indices for the modes in waveguide 1 and waveguide 2 are plotted by dotted green and orange curves, respectively. The effective indices for the modes in waveguide 3 are plotted by solid blue curves. Their effective indices cross with the effective index of waveguide 1 at 30 and 60 μm, respectively. The inset in Fig. 5(a) shows a magnified plot at the first avoided crossing so that differences in effective indices may be easily distinguished. This index matching explains the avoided crossing and coupling of the modes in waveguide 3 when W_{core2} is 30 μm or 60 μm. If W_{core2} further increases, more couplings will occur when W_{core2} is a multiple of W_{core1}, which corresponds to the coupling between the fundamental mode in the first air core and an HOM in the second air core in waveguide 3. Figure 5(b) shows a magnified plot of Fig. 5(a) so that the differences in mode profiles near the first avoided crossing may be illustrated. The insets show mode profiles when W_{core2} is 29.95 μm, 30 μm, or 30.05 μm. The solid blue curves in Fig. 5(b) show the mode indices in waveguide 3. The dashed red curves show the effective indices using Eq. (28). The two methods agree well. When $W_{\mathrm{core2}} < 30$ μm, the modes are well confined in one of the air-core layers. When $W_{\mathrm{core2}} = 30$ μm, where the avoided crossing occurs, the two modes couple with each other and become a hybrid even or odd mode, which is located in both air cores. When $W_{\mathrm{core2}} > 30$ μm, the coupling disappears and the two modes change places between the two air layers.

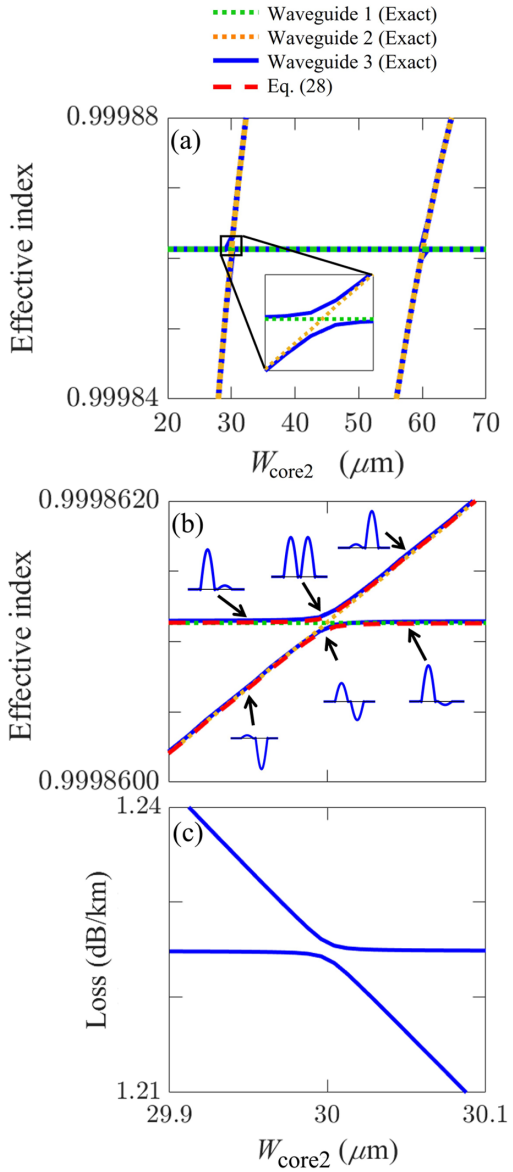

Fig. 5. (a) Effective index for the fundamental core mode in waveguides 1 and 2 (dotted curves). Effective indices for the two fundamental core modes in waveguide 3 (solid curves). (b) Magnified plot in (a) around the first avoided crossing at $W_{\mathrm{core2}} = 30$ μm. Insets show the mode in waveguide 3 around the avoided crossing with different W_{core2}. The dashed red curves show results using Eq. (28). (c) Leakage loss of the hybrid modes in waveguide 3 at the first avoided crossing.

Figure 5(c) shows that the leakage loss curves calculated using the FDM for the modes in waveguide 3 also exhibit an avoided crossing. As shown in Figs. 5(a) and 5(b), one of the two coupled modes always resides in the wider air layer and has a larger effective index, as the core size in W_{core2} increases. The leakage loss for the modes confined in the core is dominated by the core size, when the same antiresonant layers are used. Hence, the mode that resides in the wider air layer always has lower leakage loss, which leads to an avoided crossing in the leakage loss curves.

Next, we study the impact of glass layer thickness, t, on the width of the avoided crossing, δ, in waveguide 3. We fix W_{core1} and W_{core2} at 30 μm. We show the results in Fig. 6. The solid blue and dashed red curves show the width of the avoided crossing as the glass thickness varies. The solid blue curve shows the computationally exact result, while the dashed red curve shows the result from Eq. (29). The solid orange curve represents the loss. When the glass thickness is near 0.72 and 1.2 μm, which corresponds to antiresonance, the mode loss is low, and the width of the avoided crossing is small due to weak coupling. When the glass thickness is 0.95 μm, the resonance condition is

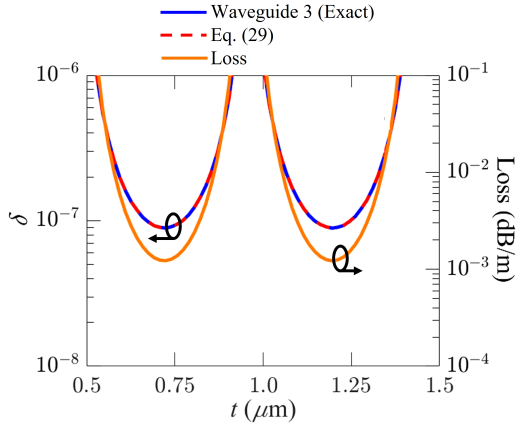

Fig. 6. Width of the avoided crossing and loss at the avoided crossing as a function of glass thickness with $g = 2$ μm and $W_{\mathrm{core1}} = W_{\mathrm{core2}} = 30$ μm.

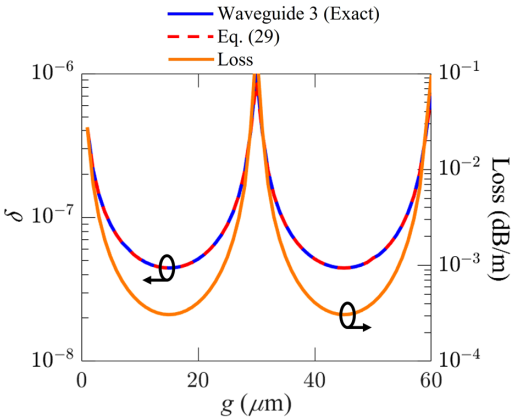

Fig. 7. Width of the avoided crossing and loss during an avoided crossing as a function of the width of air gap g with $t = 0.72$ μm and $W_{\text{core1}} = W_{\text{core2}} = 30$ μm.

satisfied, which leads to a large avoided crossing width and high loss.

We also study different gap sizes and show results in Fig. 7. The glass thickness is now fixed at 0.72 μm. The solid blue and dashed red curves show respectively the computationally exact result and the result from Eq. (29) for the avoided crossing width in waveguide 3. The solid orange curve represents loss. When the air gap approaches a multiple of $W_{\text{core1}} = W_{\text{core2}} = 30$ μm, coupling between the air mode in the core and HOM in the air gap becomes strong, the loss increases, and the width of avoided crossing increases.

6. AVOIDED CROSSINGS IN OPTICAL FIBERS

Previous sections describe avoided crossings for guided modes and leaky modes in slab waveguides where the modes can be described analytically. Avoided crossings play an important role in solid-core photonic crystal fibers [29], PBGFs [30–34], negative curvature fibers [19–21], and kagome fibers [35], where simple analytical expressions for the modes do not exist and the modes must be found computationally. This section discusses two examples of avoided crossings in solid-core and air-core photonic crystal fibers. We then describe the similarities and differences between avoided crossings in optical fibers and the simpler slab waveguides that we have analyzed in detail.

Jansen *et al.* [29] studied a large pitch photonic crystal fiber (LPF) as shown in Fig. 8. The pitch, Λ, diameter of hole, d, and wavelength are 30 μm, 0.9 μm, and 1.03 μm, respectively. The motivation to use an LPF with a large mode area comes from the requirement for high average output power. The advantage of using an LPF is that the HOMs are delocalized from the core, which leads to a reduction in the excitation of HOMs from a near-Gaussian beam, as well as increased loss for the HOMs [29]. Jansen *et al.* [29] also showed that different pump core diameters, bending radii, and/or index depression may lead to avoided crossings that manifest themselves in unwanted deformations of the output beam. Figure 9 shows three avoided crossings in the effective index curves for the fundamental mode and the HOMs. As the air-clad diameter increases, the transverse mode profiles switch between modes. The same switching behavior is present in the slab waveguides that we analyzed in

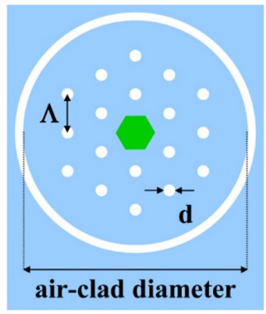

Fig. 8. Schematic structure of a rare-earth-doped (green region) double-clad LPF. Reprinted with permission from [29]. Copyright 2011 Optical Society of America.

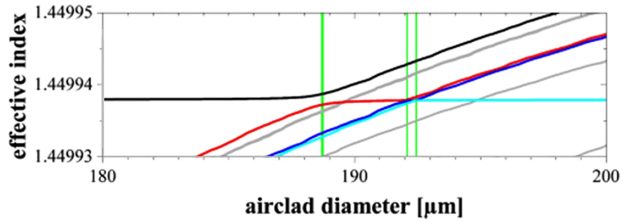

Fig. 9. Detailed plot of one broad and two narrow avoided crossings (marked in green vertical lines). The modes involved in avoided crossings are shown in black, red, green, and blue. Reprinted with permission from [29]. Copyright 2011 Optical Society of America.

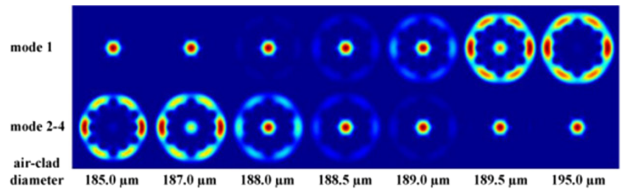

Fig. 10. Transverse mode profiles of the modes involved in the broad avoided crossing in Fig. 9 around an air-clad diameter of 188.5 μm. Across the avoided crossing, the former fundamental mode evolves into an HOM, and an HOM takes over the role as the fundamental mode. Reprinted with permission from [29]. Copyright 2011 Optical Society of America.

previous sections and is generally present in any system with avoided crossings. Figure 10 shows the evolution of the transverse mode profiles at the first avoided crossing. As the air-clad diameter changes from 185 to 195 μm, the fundamental mode evolves to the HOM and the HOM profile completely switches places from the cladding to the core. The mode-switching that we show in Figs. 9 and 10 for solid-core LPFs is analogous to the mode-switching that we show in Figs. 2 and 5 for slab waveguides.

Hollow-core fibers may also exhibit avoided crossings. A large core size is often used in hollow-core fibers to lower the fiber loss. At the same time, HOMs may exist in fibers with a large core. It is preferable to suppress higher-order core modes while preserving low leakage loss for the fundamental core mode [19,42]. This approach is analogous to using resonant coupling between the core modes and defect modes in PBGFs [30–34]. The work by Uebel *et al.* [42] optimized the ratio

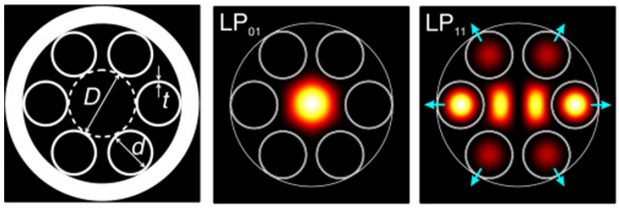

Fig. 11. (a) Sketch of the structure, with the key dimensions marked in core diameter D, capillary inner diameter d, and wall thickness t. (b) Fundamental LP_{01} mode is strongly confined. (c) HOMs experience high loss because they are coupled to modes in the capillaries. Light in the core leaks out to the solid glass sheath (indicated by blue arrows). Reprinted with permission from [42]. Copyright 2016 Optical Society of America.

of the capillary tube diameter, d, to the air-core diameter, D so that an avoided crossing between higher-order core modes and fundamental tube modes leads to an increase in the loss of higher-order core modes. Figure 11(a) shows the cross section of the negative curvature fiber considered along with illustrations for parameters d and D. Figures 11(b) and 11(c) show the transverse mode profiles for the fundamental mode and first HOM, respectively.

Figure 12(a) shows the effective indices of the fundamental mode in orange, the first HOM in blue, and the antiresonant element (ARE) mode in red. The effective indices for the HOM and ARE mode exhibit an avoided crossing at a ratio $d/D = 0.68$. Figure 12(b) shows the loss for the fundamental mode, HOM, and ARE mode. At the ratio $d/D = 0.68$, the HOM loss exponentially increases while the fundamental mode loss stays low. To quantify the suppression of HOMs, Uebel *et al.* [42] introduced a figure of merit (FOM) as $\mathrm{FOM}_{lm} = \alpha_{lm}/\alpha_{01} - 1$, where α_{lm} is the loss for the LP_{lm} mode in dB/m, and α_{01} is the loss of the fundamental core mode. The gray-shaded area in Fig. 12(b) shows the region where $\mathrm{FOM}_{11} > 20$. Figure 12(c) shows a magnified plot of the avoided crossing between the HOM and the ARE mode.

In two-dimensional air-core bandgap fibers, West *et al.* [31] showed that loss is related to the width of the avoided crossing between the air-core mode and the surface modes supported at the core–cladding interface, which is consistent to what appears in Fig. 12 near the avoided crossing. Hence, the width of an avoided crossing is a key parameter in determining the loss of the fundamental core mode. Debord *et al.* [35] observed and analyzed a similar avoided crossing in kagome fibers.

In both solid-core and air-core optical fibers, the core mode couples strongly to other core modes and cladding modes under certain conditions. The analysis of avoided crossings is useful in determining mode coupling and the loss of the core mode in specialty solid-core and hollow-core fibers when coupling occurs between the core mode and cladding modes. Due to the complexity in design of many modern-day specialty fibers, numerical solutions must be employed to calculate the effective indices and observe the avoided crossings. However, the basic switching behavior and its dependence on the width of the avoided crossing are unchanged.

There are differences in the leakage loss curves during avoided crossings between the slab waveguides and optical fibers. Because the slab waveguide is a one-dimensional structure, the leakage loss is dominated by the core size, meaning that one of the two modes will always have a higher loss as we change W_{core2} during the avoided crossing, as shown in Fig. 5. Hence, one of the two coupled modes always has lower loss compared to the other coupled mode, and an avoided crossing is manifested in the leakage loss curves in Fig. 5(c). In two-dimensional structures, such as specialty optical fibers, the mode in the cladding has a higher loss than the mode in the core. Hence, the leakage loss curves in Fig. 12(b) cross, rather than form an avoided crossing.

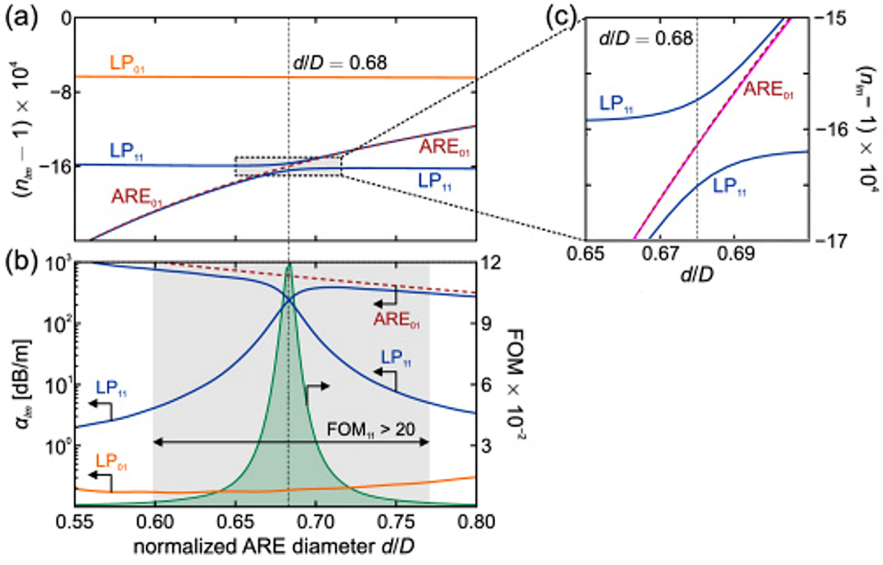

Fig. 12. (a) Modal refractive indices of the LP_{01} (orange) and even and odd LP_{11} (blue) modes. (b) Modal losses and FOM_{11} (green). The brown dashed curves in each plot refer to the antiresonant element (ARE) mode of an isolated ARE capillary. For optimal HOM suppression, $d/\Lambda = 0.68$. The geometrical parameters are $t/D = 0.01$ and $D/\lambda = 20$. The gray-shaded area in (b) shows the region where $\mathrm{FOM}_{11} > 20$. (c) Magnified plot of the avoided crossing in (a). Reprinted with permission from [42]. Copyright 2016 Optical Society of America.

7. SUMMARY

In this tutorial, we present coupled-mode theory in slab waveguides for both guided modes in index-guided waveguides and leaky modes in antiresonant waveguides. The theory for the former is classical and covered in many textbooks, but the latter is not. Our goal is to emphasize the analogy between these two waveguide types. Antiresonant photonic crystal fibers have become important in applications, but geometries are too complex to be simply analyzed. For both waveguide types, we considered a geometry with two cores. For the index-guided waveguide, the two cores are separated and surrounded by a lower-index cladding. For the antiresonant waveguide, the two air cores are separated from each other and from the air cladding by double-glass partitions. Although the modes in antiresonant waveguides are leaky, the theoretical development to determine the mode coupling near an avoided crossing is almost identical. Antiresonance implies that the avoided crossings are weak and the modes are well confined to the cores. This behavior is analogous to guided-mode waveguides with a large gap between cores. When the modes are well confined, leakage is low, and hence so is the loss. The correlation between loss and width of the avoided crossing is important in applications to photonic crystal fibers since it is usually desirable to have low loss. There is no analogous loss mechanism in index-guided waveguides. Coupled-mode theory accurately predicts the magnitude of avoided crossings, and their locations as parameters vary for both waveguide types.

In conclusion, we have shown that it is possible to explain the principal features of avoided crossings in index-guided and antiresonant waveguides using a simple slab waveguide model. We have also shown that a coupled-mode theory close to the standard theory for guided modes can be used to predict the behavior of avoided crossings for leaky modes. We discussed examples of avoided crossings in solid-core and air-core optical fibers. We described the similarities and differences between specialty optical fibers and the simpler slab waveguides that we have analyzed in detail. Thus, this model is a useful basis for understanding avoided crossings in the more complex geometries typically found in photonic crystal fibers.

Funding. National Science Foundation (1809622).

Disclosures. The authors declare no conflicts of interest.

Data Availability. Data underlying the results presented in this paper are not publicly available at this time but may be obtained from the authors upon reasonable request.

REFERENCES

1. J. Hu and C. R. Menyuk, "Understanding leaky modes: slab waveguide revisited," Adv. Opt. Photon. **1**, 58–106 (2009).
2. A. Yariv, *Quantum Electronics* (Wiley, 1989).
3. L. A. Coldren, S. W. Corzine, and M. L. Mašanović, *Diode Lasers and Photonic Integrated Circuits*, 2nd ed. (Wiley, 2012).
4. R. Marchetti, C. Lacava, L. Carroll, K. Gradkowski, and P. Minzioni, "Coupling strategies for silicon photonics integrated chips [Invited]," Photon. Res. **7**, 201–239 (2019).
5. H. Sakr, Y. Chen, G. T. Jasion, T. D. Bradley, J. R. Hayes, H. C. H. Mulvad, I. A. Davidson, E. N. Fokoua, and F. Poletti, "Hollow core optical fibres with comparable attenuation to silica fibres between 600 and 1100 nm," Nat. Commun. **11**, 6030 (2020).
6. H. Sakr, T. D. Bradley, G. T. Jasion, E. N. Fokoua, S. R. Sandoghchi, I. A. Davidson, A. Taranta, G. Guerra, W. Shere, Y. Chen, J. R. Hayes, D. J. Richardson, and F. Poletti, "Hollow core NANFs with five nested tubes and record low loss at 850, 1060, 1300 and 1625nm," in *Optical Fiber Communications Conference and Exhibition (OFC)* (2021), paper F3A.4.
7. T. D. Bradley, G. T. Jasion, H. Sakr, I. A. Davidson, J. R. Hayes, A. Taranta, K. Harrington, E. N. Fokoua, Y. Chen, D. J. Richardson, and F. Poletti, "Towards low loss hollow core optical fibers," Proc. SPIE **11713**, 117130A (2021).
8. F. Amrani, J. H. Osório, F. Delahaye, F. Giovanardi, L. Vincetti, B. Debord, F. Gérôme, and F. Benabid, "Low-loss single-mode hybrid-lattice hollow-core photonic-crystal fibre," Light Sci. Appl. **10**, 7 (2021).
9. T. D. Bradley, J. R. Hayes, Y. Chen, G. T. Jasion, S. R. Sandoghchi, R. Slavik, E. N. Fokoua, S. Bawn, H. Sakr, I. A. Davidson, A. Taranta, J. P. Thomas, M. N. Petrovich, D. J. Richardson, and F. Poletti, "Record low-loss 1.3 dB/km data transmitting antiresonant hollow core fibre," in *European Conference on Optical Communication (ECOC)* (2018), pp. 1–3.
10. T. D. Bradley, G. T. Jasion, J. R. Hayes, Y. Chen, L. Hooper, H. Sakr, M. Alonso, A. Taranta, A. Saljoghei, H. C. Mulvad, M. Fake, I. A. Davidson, N. Wheeler, E. N. Fokoua, W. Wang, S. R. Sandoghchi, D. Richardson, and F. Poletti, "Antiresonant hollow core fibre with 0.65 dB/km attenuation across the C and L telecommunication bands," in *45th European Conference on Optical Communication (ECOC)* (2019), pp. 1–4.
11. G. T. Jasion, T. D. Bradley, K. Harrington, H. Sakr, Y. Chen, E. N. Fokoua, I. A. Davidson, A. Taranta, J. R. Hayes, D. J. Richardson, and F. Poletti, "Hollow core NANF with 0.28 dB/km attenuation in the C and L bands," in *Optical Fiber Communication Conference Postdeadline Papers* (Optical Society of America, 2020), paper Th4B.4.
12. M. Michieletto, J. K. Lyngsø, C. Jakobsen, J. Lægsgaard, O. Bang, and T. T. Alkeskjold, "Hollow-core fibers for high power pulse delivery," Opt. Express **24**, 7103–7119 (2016).
13. J. D. Shephard, A. Urich, R. M. Carter, P. Jaworski, R. R. J. Maier, W. Belardi, F. Yu, W. J. Wadsworth, J. C. Knight, and D. P. Hand, "Silica hollow core microstructured fibers for beam delivery in industrial and medical applications," Front. Phys. **3**, 24 (2015).
14. F. Giovanardi, A. Cucinotta, A. Rozzi, R. Corradini, F. Benabid, L. Rosa, and L. Vincetti, "Hollow core inhibited coupling fibers for biological optical sensing," J. Lightwave Technol. **37**, 2598–2604 (2019).
15. F. Benabid, J. Knight, G. Antonopoulos, and P. St.J. Russell, "Stimulated Raman scattering in hydrogen-filled hollow-core photonic crystal fiber," Science **298**, 399–402 (2002).
16. A. V. V. Nampoothiri, A. M. Jones, C. Fourcade-Dutin, C. Mao, N. Dadashzadeh, B. Baumgart, Y. Y. Wang, M. Alharbi, T. Bradley, N. Campbell, F. Benabid, B. R. Washburn, K. L. Corwin, and W. Rudolph, "Hollow-core optical fiber gas lasers (HOFGLAS): a review [Invited]," Opt. Mater. Express **2**, 948–961 (2012).
17. F. Couny, F. Benabid, and P. S. Light, "Subwatt threshold cw Raman fiber-gas laser based on H_2-filled hollow-core photonic crystal fiber," Phys. Rev. Lett. **99**, 143903 (2007).
18. R. Sollapur, D. Kartashov, M. Zürch, A. Hoffmann, T. Grigorova, G. Sauer, A. Hartung, A. Schwuchow, J. Bierlich, J. Kobelke, M. Chemnitz, M. A. Schmidt, and C. Spielmann, "Resonance-enhanced multi-octave supercontinuum generation in antiresonant hollow-core fibers," Light Sci. Appl. **6**, e17124 (2017).
19. C. Wei, R. A. Kuis, F. Chenard, C. R. Menyuk, and J. Hu, "Higher-order mode suppression in chalcogenide negative curvature fibers," Opt. Express **23**, 15824–15832 (2015).
20. C. Wei, C. R. Menyuk, and J. Hu, "Polarization-filtering and polarization-maintaining low-loss negative curvature fibers," Opt. Express **26**, 9528–9540 (2018).
21. L. Provino, "Effect of nested elements on avoided crossing between the higher-order core modes and the air-capillary modes in hollow-core antiresonant optical fibers," Fibers **6**, 42 (2018).
22. W. Bogaerts, P. D. Heyn, T. V. Vaerenbergh, K. D. Vos, S. K. Selvaraja, T. Claes, P. Dumon, P. Bienstman, D. V. Thourhout, and R. Baets, "Silicon microring resonators," Laser Photon. Rev. **6**, 47–73 (2012).

23. J. von Neumann and E. P. Wigner, "Über merkwürdige diskrete Eigenwerte," Phys. Z. **30**, 465–467 (1929).
24. R. S. Mulliken, "Solved and unsolved problems in the spectra of diatomic molecules," J. Phys. Chem. **41**, 5–45 (1937).
25. A. G. Gaydon and W. G. Penney, "The dissociation energies of CO, N_2, NO and CN," Proc. R. Soc. London Ser. A **183**, 374–388 (1945).
26. T. G. Eck, L. L. Foldy, and H. Wieder, "Observation of "anticrossings" in optical resonance fluorescence," Phys. Rev. Lett. **10**, 239–242 (1963).
27. D. Marcuse and I. P. Kaminow, "Modes of a symmetric slab optical waveguide in birefringent media, part II: slab with coplanar optical axis," IEEE J. Quantum Electron. **15**, 92–101 (1979).
28. R. J. Spreeuw, J. P. Woerdman, and D. Lenstra, "Photon band structure in a Sagnac fiber-optic ring resonator," Phys. Rev. Lett. **61**, 318–321 (1988).
29. F. Jansen, F. Stutzki, C. Jauregui, J. Limpert, and A. Tünnermann, "Avoided crossings in photonic crystal fibers," Opt. Express **19**, 13578–3589 (2011).
30. C. M. Smith, N. Venkataraman, M. T. Gallagher, D. Müller, J. A. West, N. F. Borrelli, D. C. Allan, and K. W. Koch, "Low-loss hollow-core silica/air photonic bandgap fibre," Nature **424**, 657–659 (2003).
31. J. A. West, C. M. Smith, N. F. Borrelli, D. C. Allan, and K. W. Koch, "Surfaces modes in air-core photonic band-gap fibers," Opt. Express **12**, 1485–1496 (2004).
32. K. Saitoh, N. A. Mortensen, and M. Koshiba, "Air-core photonic band-gap fibers: the impact of surface modes," Opt. Express **12**, 394–400 (2004).
33. J. Hu and C. R. Menyuk, "Leakage loss and bandgap analysis in air-core photonic bandgap fiber for nonsilica glasses," Opt. Express **15**, 339–349 (2007).
34. J. M. Fini, J. W. Nicholson, B. Mangan, L. Meng, R. S. Windeler, E. M. Monberg, A. DeSantolo, F. V. DiMarcello, and K. Mukasa, "Polarization maintaining single-mode low-loss hollow-core fibres," Nat. Commun. **5**, 5085 (2014).
35. B. Debord, F. Amrani, L. Vincetti, F. Gérôme, and F. Benabid, "Hollow-core fiber technology: the rising of "gas photonics," Fibers **7**, 16 (2019).
36. D. Noordegraaf, L. Scolari, J. Lægsgaard, T. T. Alkeskjold, G. Tartarini, E. Borelli, P. Bassi, J. Li, and S.-T. Wu, "Avoided-crossing-based liquid-crystal photonic-bandgap notch filter," Opt. Lett. **33**, 986–988 (2008).
37. T. Han, Y.-G. Liu, Z. Wang, B. Zou, B. Tai, and B. Liu, "Avoided-crossing-based ultrasensitive photonic crystal fiber refractive index sensor," Opt. Lett. **35**, 2061–2063 (2010).
38. B. Shuai, L. Xia, Y. Zhang, and D. Liu, "A multi-core holey fiber based plasmonic sensor with large detection range and high linearity," Opt. Express **20**, 5974–5986 (2012).
39. A. Hassani and M. Skorobogatiy, "Surface plasmon resonance-like integrated sensor at terahertz frequencies for gaseous analytes," Opt. Express **16**, 20206–20214 (2008).
40. J. Zuo, T. Han, J. Yang, Y. Chen, Y.-G. Lin, and J. Cai, "High sensitivity temperature sensor with an avoided-crossing based selective-filling high birefringent photonic crystal fiber Sagnac interferometer," IEEE Access **6**, 45527–45533 (2018).
41. F. Poli, E. Coscelli, T. T. Alkeskjold, D. Passaro, A. Cucinotta, L. Leick, J. Broeng, and S. Selleri, "Cut-off analysis of 19-cell Yb-doped double-cladding rod-type photonic crystal fibers," Opt. Express **19**, 9896–9907 (2011).
42. P. Uebel, M. C. Günendi, M. H. Frosz, G. Ahmed, N. N. Edavalath, J.-M. Ménard, and P. St.J. Russell, "Broadband robustly single-mode hollow-core PCF by resonant filtering of higher-order modes," Opt. Lett. **41**, 1961–1964 (2016).
43. N. M. Litchinitser, A. K. Abeeluck, C. Headley, and B. J. Eggleton, "Antiresonant reflecting photonic crystal optical waveguides," Opt. Lett. **27**, 1592–1594 (2002).
44. C. Wei, R. J. Weiblen, C. R. Menyuk, and J. Hu, "Negative curvature fibers," Adv. Opt. Photon **9**, 504–561 (2017).
45. C. Wei, J. Hu, and C. R. Menyuk, "Comparison of loss in silica and chalcogenide negative curvature fibers as the wavelength varies," Front. Phys. **4**, 30 (2016).
46. M. A. Duguay, Y. Kokubun, T. L. Koch, and L. Pfeiffer, "Antiresonant reflecting optical waveguides in SiO_2-Si multilayer structures," Appl. Phys. Lett. **49**, 13–15 (1986).